Journal of Sound and Vibration (1997) **207**(4), 497–520

DYNAMIC STABILITY OF CYLINDRICAL SHELLS SUBJECTED TO CONSERVATIVE PERIODIC AXIAL LOADS USING DIFFERENT SHELL THEORIES

K. Y. Lam and T. Y. Ng

Department of Mechanical and Production Engineering, National University of Singapore, 10 Kent Ridge Crescent, Singapore 119260

(*Received* 17 *September* 1996, *and in final form* 2 *April* 1997)

In the present paper, the dynamic stability of thin, isotropic cylindrical shells under combined static and periodic axial forces is studied using four common thin shell theories; namely, the Donnell, Love, Sanders and Flugge shell theories. For these four cases, the contribution of the stresses due to the external axial forces are accounted for according to the Donnell theory. In the present analysis, a normal-mode expansion of the equations of motion yields a system of Mathieu–Hill equations, the stability of which is examined. The parametric resonance responses are analyzed based on Bolotin's method and the effects of the length-to-radius and thickness-to-radius ratios of the cylinder on the instability regions are examined and compared using the four theories. The effects of variation in the magnitude of the axial forces were also examined.

1. INTRODUCTION

Structural components under the influence of periodic loads may undergo parametric resonance which can occur over a range or ranges of forcing frequencies. If the load is compressive to the structure, resonance or instability can occur and usually does occur even if the magnitude of the load is below the critical buckling load of the structure. It is thus of great technical importance to clarify the dynamic stability of dynamic systems under periodic loads. The parametric resonance of cylindrical shells under axial loads has become a popular subject of study, and was first treated by Bolotin [1], Yao [2] and Vijayaraghavan and Evan-Iwanowski [3]. For thin cylindrical shells under periodic axial loads, the method of solution is usually first to reduce the equations of motion to a system of Mathieu–Hill equations. The dynamic stability for such a system of Mathieu–Hill equations is then analyzed by a number of methods. The instability regions can be divided into four classes; namely, first order parametric resonances, higher order parametric resonances, sum combination resonances and difference combination resonances. The first two are sometimes called direct parametric resonances and the other two are sometimes simply referred to as combination resonances. A detailed study of combination resonances with reference to transverse, axial and circumferential waves is given in Korval [4], using the Donnell shell theory.

The monodromy matrix method was used by Argento and Scott [5, 6] and Argento [7], in their series of papers, to determine the instability regions of a composite circular cylindrical shell subjected to combined axial and torsional loading. The Donnell theory was employed in their papers. The harmonic balance method was used by Takahashi and Konishi [8] and Takahashi *et al*. [9] to investigate the dynamic stability of parametric

0022–460X/97/440497 + 24 $25.00/0/sv971186

dynamic systems subjected to inplane dynamic forces. These two methods are, however, very numerically intensive. An alternative perturbation procedure, restricted to only very small loadings and known as Hsu's method, is less intensive and also determines all instabilities. Nagai and Yamaki [10] used this method together with the Donnell shell theory to study the dynamic stability of cylindrical shells under periodic compressive forces. For direct parametric resonances, the simple and well-known method due to Bolotin [1] reduces the system of Mathieu–Hill equations to the standard form of a generalized eigenvalue problem, in which solutions are easily computed.

A literature search showed that a study comparing the instability regions generated using the Donnell, Love, Sanders and Flugge shell theories for an axially loaded circular cylindrical shell is not available. Such a study would be interesting and useful, as it might shed light on the relative accuracies of these theories in predicting the widths of the unstable regions. However, such studies have been carried out by Lam and Loy [11, 12] using the Love theory for the free vibration of a rotating multi-layered cylindrical shell, and the four different shell theories were also employed by Lam and Loy [13] for the same problem in a study to investigate the relative accuracies of the different theories. In the present analysis, the dynamic stability of thin, isotropic cylindrical shells under combined static and periodic axial forces is studied using the four different shell theories—those due to Donnell, Love, Sanders and Flugge. For each case, the present formulation treats the small vibration displacements according to each shell theory but takes into account the contribution of the stresses due to the external axial forces according to the Donnell theory. A normal-mode expansion yields a system of Mathieu–Hill equations and the parametric resonance response are analyzed based on Bolotin's method. The present formulation of the problem is also made general to accommodate any boundary conditions but, for reasons of simplicity, the comparison study is only carried out for the case of simply supported boundary conditions. Numerical results of the instability regions are presented for various length and thickness-to-radius ratios of the cylindrical shell.

2. THEORY AND FORMULATION

The cylindrical shell as shown in Figure 1 is assumed to be a thin, uniform shell of length L, thickness h and radius R. The x-axis is taken along a generator, the circumferential arc length subtends an angle θ, and the z-axis is directed radially inwards. The pulsating axial load is given by

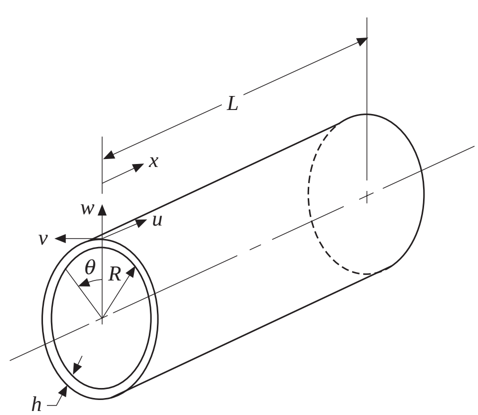

Figure 1. The co-ordinate system of the circular cylindrical shell.

$$N(x, t) = N_0 + N_a \cos pt, \tag{1}$$

where p is the frequency of excitation in radians per unit time.

For this analysis, four shell theories for a thin-walled cylindrical shell are compared. They are the Donnell, Love, Sanders and Flugge theories for thin cylindrical shells. The equations of motion for thin cylindrical shells under the pulsating load given in equation (1) can be written in matrix form as

$$[\mathscr{L}]\,\{u_i\} = \{0\} \tag{2}$$

where $\{u_i\}$ is the displacement vector

$$\{u_i\} = \begin{bmatrix} u \\ v \\ w \end{bmatrix}, \tag{3}$$

and u, v and w are the orthogonal components in the x, θ and radial directions respectively, and $\mathscr{L}$ is a matrix differential operator.

The $\mathscr{L}$ operator can be treated as the sum of two operators

$$[\mathscr{L}] = [\mathscr{L}_D] + k^2[\mathscr{L}_{MOD}] \tag{4}$$

where $[\mathscr{L}_D]$ is the differential operator according to the Donnell theory, $[\mathscr{L}_{MOD}]$ is a "modifying" operator that alters the Donnell operator to yield another shell theory, and k is the non-dimensional thickness parameter, defined as

$$k = \left(\frac{h^2}{12R^2}\right)^{1/2} \tag{5}$$

The following non-dimensionalized parameters are introduced to simplify the formulation:

$$\alpha = x/R, \qquad l = L/R, \tag{6}$$

$$\eta_0 = \frac{N_0\,(1 - v^2)}{Eh}, \qquad \eta_a = \frac{N_a\,(1 - v^2)}{Eh} \tag{7}$$

and

$$\bar{p} = p\left(\frac{\rho h R^2}{C}\right)^{1/2}, \qquad \Omega = \omega\left(\frac{\rho h R^2}{C}\right)^{1/2}, \tag{8}$$

where ω is the natural frequency of the cylindrical shell under the constant axial load N_0, with the oscillating component $N_a = 0$, and

$$\tau = t\left(\frac{C}{\rho h R^2}\right)^{1/2}, \qquad C = \frac{Eh}{1 - v^2}. \tag{9}$$

Thus, equation (1) can be written as

$$\eta(\alpha, \tau) = \eta_0 + \eta_a \cos \bar{p}\tau \tag{10}$$

and the Donnell operator for thin cylindrical shells under the pulsating load given in equation (10) takes the form

$$[\mathscr{L}_D] = \begin{bmatrix} \left[\dfrac{\partial^2}{\partial \alpha^2} + \dfrac{1-v}{2}\dfrac{\partial^2}{\partial \theta^2} - \dfrac{\partial^2}{\partial \tau^2}\right] & \dfrac{1+v}{2}\dfrac{\partial^2}{\partial \alpha\, \partial \theta} & v\dfrac{\partial}{\partial \alpha} \\ \dfrac{1+v}{2}\dfrac{\partial^2}{\partial \alpha\, \partial \theta} & \left[\dfrac{1-v}{2}\dfrac{\partial^2}{\partial x^2} + \dfrac{\partial^2}{\partial \theta^2} - \dfrac{\partial^2}{\partial \tau^2}\right] & \dfrac{\partial}{\partial \theta} \\ -v\dfrac{\partial}{\partial x} & -\dfrac{\partial}{\partial \theta} & \left[-1 - k^2 \nabla^4 + \dfrac{\partial}{\partial \alpha}\left(\eta \dfrac{\partial}{\partial \alpha}\right) - \dfrac{\partial^2}{\partial \tau^2}\right] \end{bmatrix}, \tag{11}$$

where $\nabla^4 = \nabla^2\nabla^2$ and

$$\nabla^2 = \frac{\partial^2}{\partial\alpha^2} + \frac{\partial^2}{\partial\theta^2}. \tag{12}$$

Similarly, the modifying operators for the various cylindrical shell theories take the forms as shown below:

Love:

$$[\mathscr{L}_{MOD}] = \begin{bmatrix} 0 & 0 & 0 \\ 0 & (1-\nu)\dfrac{\partial^2}{\partial\alpha^2} + \dfrac{\partial^2}{\partial\theta^2} & -\dfrac{\partial^3}{\partial\alpha^2\,\partial\theta} - \dfrac{\partial^3}{\partial\theta^3} \\ 0 & -(2-\nu)\dfrac{\partial^3}{\partial\alpha^2\,\partial\theta} - \dfrac{\partial^3}{\partial\theta^3} & 0 \end{bmatrix}. \tag{13}$$

Sanders:

$$[\mathscr{L}_{MOD}] = \begin{bmatrix} \dfrac{1-\nu}{8}\dfrac{\partial^2}{\partial\theta^2} & -\dfrac{3(1-\nu)}{8}\dfrac{\partial^2}{\partial\alpha\,\partial\theta} & \dfrac{1-\nu}{2}\dfrac{\partial^3}{\partial\alpha\,\partial\theta^2} \\ -\dfrac{3(1-\nu)}{8}\dfrac{\partial^2}{\partial\alpha\,\partial\theta} & \dfrac{9(1-\nu)}{8}\dfrac{\partial^2}{\partial\alpha^2} + \dfrac{\partial^2}{\partial\theta^2} & -\dfrac{3-\nu}{2}\dfrac{\partial^3}{\partial\alpha^2\,\partial\theta} - \dfrac{\partial^3}{\partial\theta^3} \\ -\dfrac{1-\nu}{2}\dfrac{\partial^3}{\partial\alpha\,\partial\theta^2} & \dfrac{3-\nu}{2}\dfrac{\partial^3}{\partial\alpha^2\,\partial\theta} + \dfrac{\partial^3}{\partial\theta^3} & 0 \end{bmatrix}. \tag{14}$$

Flugge:

$$[\mathscr{L}_{MOD}] = \begin{bmatrix} \dfrac{1-\nu}{2}\dfrac{\partial^2}{\partial\theta^2} & 0 & -\dfrac{\partial^3}{\partial\alpha^3} + \dfrac{1-\nu}{2}\dfrac{\partial^3}{\partial\alpha\,\partial\theta^2} \\ 0 & \dfrac{3(1-\nu)}{2}\dfrac{\partial^2}{\partial\alpha^2} & -\dfrac{3-\nu}{2}\dfrac{\partial^3}{\partial\alpha^2\,\partial\theta} \\ \dfrac{\partial^3}{\partial\alpha^3} - \dfrac{1-\nu}{2}\dfrac{\partial^3}{\partial\alpha\,\partial\theta^2} & \dfrac{3-\nu}{2}\dfrac{\partial^3}{\partial\alpha^2\,\partial\theta} & -1 - 2\dfrac{\partial^2}{\partial\theta^2} \end{bmatrix}. \tag{15}$$

If the shell is assumed to be simply supported, there exists a solution for the equations of motion given by the form

$$w_{mn} = A_{mn}\,\mathrm{e}^{\mathrm{i}\Omega\tau}\sin\frac{m\pi\alpha}{l}\cos n\theta, \tag{16}$$

$$v_{mn} = B_{mn}\,\mathrm{e}^{\mathrm{i}\Omega\tau}\sin\frac{m\pi\alpha}{l}\sin n\theta, \tag{17}$$

$$u_{mn} = C_{mn}\,\mathrm{e}^{\mathrm{i}\Omega\tau}\cos\frac{m\pi\alpha}{l}\cos n\theta, \tag{18}$$

where n represents the number of circumferential waves and m the number of axial half-waves in the corresponding standing wave pattern.

The equations of motion can be solved using an eigenfunction expansion in terms of the normal modes of the free vibrations of a cylindrical shell under a constant axial load N_0 with the oscillating component $N_a = 0$. Substitution of equations (16–18) into the equations of motion, which are a set of three coupled homogenous equations, yields a cubic frequency equation when the determinant is equated to zero. Thus, for each m and n, there exist three roots corresponding to the transverse, axial and circumferential modes.

To solve the equations of motion that include the oscillating component N_a, a solution is sought in the form shown below, where all of the modes are superimposed:

$$w_{mnj} = \sum_{j=1}^{3} \sum_{m=1}^{\infty} \sum_{n=1}^{\infty} A_{mnj}\, \bar{q}_{mnj}(\tau) \sin \lambda\alpha \cos n\theta, \tag{19}$$

$$v_{mnj} = \sum_{j=1}^{3} \sum_{m=1}^{\infty} \sum_{n=1}^{\infty} B_{mnj}\, \bar{q}_{mnj}(\tau) \sin \lambda\alpha \sin n\theta, \tag{20}$$

$$u_{mnj} = \sum_{j=1}^{3} \sum_{m=1}^{\infty} \sum_{n=1}^{\infty} C_{mnj}\, \bar{q}_{mnj}(\tau) \cos \lambda\alpha \cos n\theta, \tag{21}$$

where $\bar{q}_{mnj}(\tau)$ is a generalized co-ordinate and

$$\lambda = m\pi/l. \tag{22}$$

Substituting equations (19–21) into the equations of motion and simplifying yields

$$\sum_{j=1}^{3} \sum_{m=1}^{\infty} \sum_{n=1}^{\infty} (\ddot{\bar{q}}_{mnj} + \Omega_{mnj}^2 \bar{q}_{mnj})\Gamma_{mnj} \cos \lambda\alpha \cos n\theta = 0, \tag{23}$$

$$\sum_{j=1}^{3} \sum_{m=1}^{\infty} \sum_{n=1}^{\infty} (\ddot{\bar{q}}_{mnj} + \Omega_{mnj}^2 \bar{q}_{mnj})\beta_{mnj} \sin \lambda\alpha \sin n\theta = 0, \tag{24}$$

$$\sum_{j=1}^{3} \sum_{m=1}^{\infty} \sum_{n=1}^{\infty} (\ddot{\bar{q}}_{mnj} + \Omega_{mnj}^2 \bar{q}_{mnj}) \sin \lambda\alpha \cos n\theta - \lambda \cos \bar{p}\tau \sum_{j=1}^{3} \sum_{m=1}^{\infty} \sum_{n=1}^{\infty} \bar{q}_{mnj} \frac{\partial}{\partial\alpha}(\eta_a \cos \lambda\alpha) \cos n\theta = 0, \tag{25}$$

where

$$\beta_{mnj} = B_{mnj}/A_{mnj}, \qquad \Gamma_{mnj} = C_{mnj}/A_{mnj}. \tag{26, 27}$$

The definitions for β_{mnj} and Γ_{mnj} for the different shell theories are given in Appendix A.

Making use of the orthogonality condition, we multiply equation (23) by $\Gamma_{rsi} \cos \lambda_r \alpha \cos s\theta$, equation (24) by $\beta_{rsi} \sin \lambda_r \alpha \sin s\theta$, and equation (25) by $\sin \lambda_r \alpha \cos s\theta$. We then add the three resulting equations and integrate over the surface of the cylinder. This yields the following set of equations

$$\bar{\mathbf{M}}_{IJ}\, \ddot{\mathbf{q}}_J + (\bar{\mathbf{K}}_{IJ} - \cos \bar{p}\tau \bar{\mathbf{Q}}_{IJ})\bar{\mathbf{q}}_J = 0, \tag{28}$$

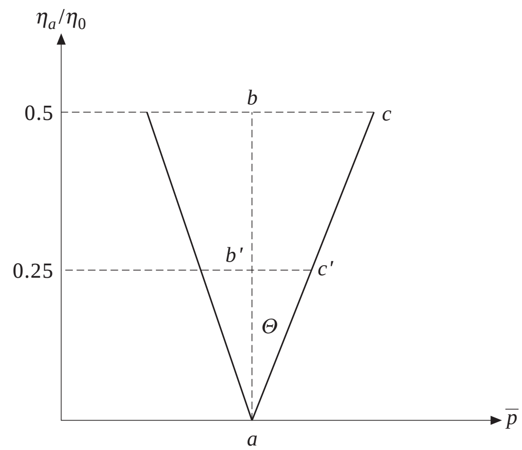

Figure 2. An unstable region in the η_a/η_0–$\bar{p}$ plane.

where $\bar{\mathbf{M}}_{IJ}$, $\bar{\mathbf{K}}_{IJ}$ and $\bar{\mathbf{Q}}_{IJ}$ are matrices and $\ddot{\bar{\mathbf{q}}}_J$ and $\bar{\mathbf{q}}_J$ are column vectors consisting of $\ddot{\bar{q}}_{mnj}$ and $\bar{q}_{mnj}$ respectively, and

$$r = 1, 2, 3, \ldots, N, \qquad s = 1, 2, 3, \ldots, N, \qquad i = 1, 2, 3,$$

$$m = 1, 2, 3, \ldots, N, \qquad n = 1, 2, 3, \ldots, N, \qquad j = 1, 2, 3,$$

$$I = 1, 2, 3, \ldots, (N \times N \times 3), \qquad J = 1, 2, 3, \ldots, (N \times N \times 3), \tag{29}$$

where for

$$\begin{aligned}
&I = 1, \quad r = 1, \quad s = 1, \quad i = 1,\\
&I = 2, \quad r = 1, \quad s = 1, \quad i = 2,\\
&I = 3, \quad r = 1, \quad s = 1, \quad i = 3,\\
&I = 4, \quad r = 1, \quad s = 2, \quad i = 1,\\
&I = 5, \quad r = 1, \quad s = 2, \quad i = 2,\\
&I = 6, \quad r = 1, \quad s = 2, \quad i = 3,\\
&I = 7, \quad r = 1, \quad s = 3, \quad i = 1,\\
&\vdots\\
&I = 3N - 2, \quad r = 1, \quad s = N, \quad i = 1,\\
&I = 3N - 1, \quad r = 1, \quad s = N, \quad i = 2,\\
&I = 3N, \quad r = 1, \quad s = N, \quad i = 3,\\
&I = 3N + 1, \quad r = 2, \quad s = 1, \quad i = 1,\\
&I = 3N + 2, \quad r = 2, \quad s = 1, \quad i = 2,\\
&I = 3N + 3, \quad r = 2, \quad s = 1, \quad i = 3,\\
&\vdots\\
&I = 3N^2 - 2, \quad r = N, \quad s = N, \quad i = 1,
\end{aligned}$$

$$I = 3N^2 - 1, \qquad r = N, \quad s = N, \quad i = 2,$$

$$I = 3N^2, \qquad r = N, \quad s = N, \quad i = 3. \tag{30}$$

The co-relations between the subscripts J, m, n and j follow those of I, r, s and i respectively. The matrices $\bar{\mathbf{M}}_{IJ}$, $\bar{\mathbf{K}}_{IJ}$ and $\bar{\mathbf{Q}}_{IJ}$ are given as

$$\bar{\mathbf{M}}_{IJ} = \int_0^l \int_0^{2\pi} (\Gamma_I \Gamma_J \cos \lambda_r \alpha \cos s\theta \cos \lambda_m \alpha \cos n\theta$$

$$+ \beta_I \beta_J \sin \lambda_r \alpha \sin s\theta \sin \lambda_m \alpha \sin n\theta + \sin \lambda_r \alpha \cos s\theta \sin \lambda_m \alpha \cos n\theta) \, d\theta \, d\alpha$$

$$= \begin{cases} \frac{1}{2} \pi l (1 + \Gamma_I \Gamma_J + \beta_I \beta_J) & \text{if } I = J, \\ 0 & \text{if } I \neq J, \end{cases} \tag{31}$$

$$\bar{\mathbf{K}}_{IJ} = \bar{\mathbf{M}}_{IJ} \, \Omega_J^2, \tag{32}$$

$$\bar{\mathbf{Q}}_{IJ} = \lambda_m \int_0^l \int_0^{2\pi} \frac{\partial}{\partial \alpha} (\eta_a \cos \lambda_m \alpha \cos n\theta) \sin \lambda_r \alpha \cos s\theta \, d\theta \, d\alpha$$

$$= \begin{cases} -\frac{1}{2} \pi l \lambda_r \lambda_m \eta_a & \text{if } I = J, \\ 0 & \text{if } I \neq J. \end{cases} \tag{33}$$

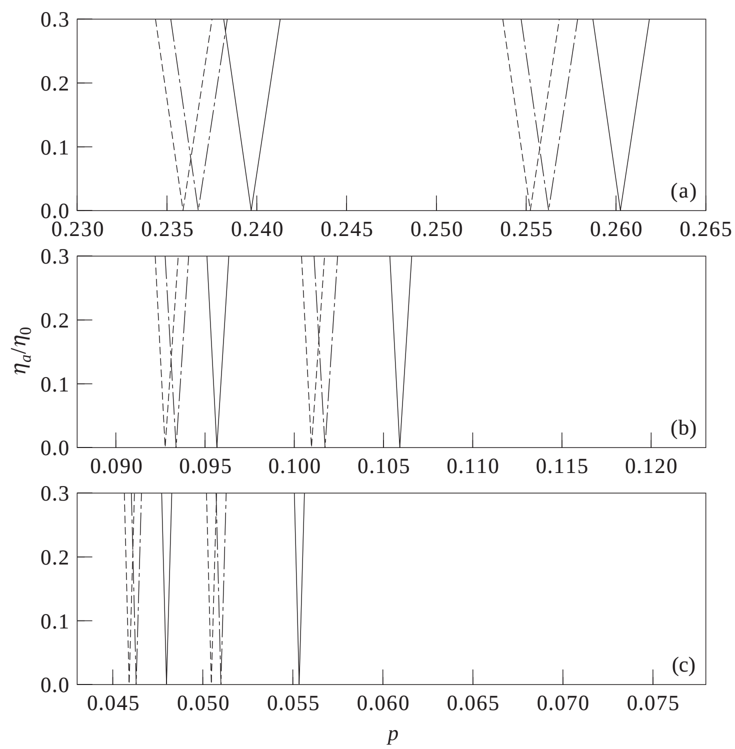

Figure 3. The first two unstable regions for a shell of thickness ratio $R/h = 100$ and under tensile loading of $\eta_0 = 0{\cdot}1\eta_{cr}$. —, Donnell, ----, Love, · · · · · , Sanders, –·–·–, Flugge. (a) $L/R = 2$; (b) $L/R = 5$; (c) $L/R = 10$.

TABLE 1

The first two unstable regions for a shell of thickness ratio $R/h = 100$ and under tensile loading of $\eta_0 = 0{\cdot}1\eta_{cr}$

		First unstable region	Second unstable region
$L/R = 2$			
Donnell	Point of origin, $\bar{p}(\times 10^{-1})$	2·3966085	2·6021009
	Angle subtended, Θ ($\times 10^{-3}$)	5·4034474	5·0480971
Love	Point of origin, $\bar{p}$ ($\times 10^{-1}$)	2·3586483	2·5526722
	Angle subtended, Θ ($\times 10^{-3}$)	5·4893049	5·1447946
Sanders	Point of origin, $\bar{p}$ ($\times 10^{-1}$)	2·3577441	2·5517569
	Angle subtended, Θ ($\times 10^{-3}$)	5·4913848	5·1466146
Flugge	Point of origin, $\bar{p}$ ($\times 10^{-1}$)	2·3668536	2·5626430
	Angle subtended, Θ ($\times 10^{-3}$)	5·4706654	5·1251351
$L/R = 5$			
Donnell	Point of origin, $\bar{p}(\times 10^{-1})$	0·9572622	1·0589963
	Angle subtended, Θ ($\times 10^{-3}$)	2·0227872	1·9205176
Love	Point of origin, $\bar{p}$ ($\times 10^{-1}$)	0·9284480	1·0101911
	Angle subtended, Θ ($\times 10^{-3}$)	2·0848530	2·0123773
Sanders	Point of origin, $\bar{p}$ ($\times 10^{-1}$)	0·9280907	1·0098113
	Angle subtended, Θ ($\times 10^{-3}$)	2·0856430	2·0131373
Flugge	Point of origin, $\bar{p}$ ($\times 10^{-1}$)	0·9338362	1·0174581
	Angle subtended, Θ ($\times 10^{-3}$)	2·0730090	1·9981973
$L/R = 10$			
Donnell	Point of origin, $\bar{p}(\times 10^{-2})$	4·7899298	5·5314616
	Angle subtended, Θ ($\times 10^{-4}$)	8·9767776	8·7983377
Love	Point of origin, $\bar{p}$ ($\times 10^{-2}$)	4·5839896	5·0410816
	Angle subtended, Θ ($\times 10^{-4}$)	9·3760173	9·6463370
Sanders	Point of origin, $\bar{p}$ ($\times 10^{-2}$)	4·5825770	5·0393022
	Angle subtended, Θ ($\times 10^{-4}$)	9·3788773	9·6497170
Flugge	Point of origin, $\bar{p}$ ($\times 10^{-2}$)	4·6179227	5·0951093
	Angle subtended, Θ ($\times 10^{-4}$)	9·3079773	9·5451971

3. STABILITY ANALYSIS

Equation (28) is in the form of a second order differential equation with periodic coefficients of the Mathieu–Hill type. Using the method presented by Bolotin [1], the regions of unstable solutions are separated by periodic solutions having period T and $2T$ with $T = 2\pi/\bar{p}$. The solutions with period $2T$ are of greater practical importance, as the widths of these unstable regions are usually larger than those associated with solutions having period T. As a first approximation, the periodic solutions with period $2T$ can be sought in the form

$$\bar{\mathbf{q}} = \mathbf{f}\sin\frac{\bar{p}\tau}{2} + \mathbf{g}\cos\frac{\bar{p}\tau}{2}, \tag{34}$$

where **f** and **g** are arbitrary vectors.

Substituting equation (34) into equation (28) and equating the coefficients of the $\sin(\bar{p}\tau/2)$ and $\cos(\bar{p}\tau/2)$ terms, a set of linear homogeneous algebraic equations in terms of **f** and **g** can be obtained. The conditions for non-trivial solutions are

$$\det\left[\begin{pmatrix} -\frac{1}{4}\bar{p}^2\bar{\mathbf{M}}_{IJ}+\bar{\mathbf{K}}_{IJ}-\frac{1}{2}\bar{\mathbf{Q}}_{IJ} & 0 \\ 0 & -\frac{1}{4}\bar{p}^2\bar{\mathbf{M}}_{IJ}+\bar{\mathbf{K}}_{IJ}+\frac{1}{2}\bar{\mathbf{Q}}_{IJ}\end{pmatrix}\right]=0. \tag{35}$$

Instead of solving the above nonlinear geometric equations for $\bar{p}$, the above expression can be rearranged in the standard form of a generalized eigenvalue problem

$$\det\left[\begin{pmatrix} \bar{\mathbf{K}}_{IJ}-\frac{1}{2}\bar{\mathbf{Q}}_{IJ} & \mathbf{0} \\ \mathbf{0} & \bar{\mathbf{K}}_{IJ}+\frac{1}{2}\bar{\mathbf{Q}}_{IJ}\end{pmatrix}-\bar{p}^2\begin{pmatrix}\frac{1}{4}\bar{\mathbf{M}}_{IJ} & \mathbf{0} \\ \mathbf{0} & \frac{1}{4}\bar{\mathbf{M}}_{IJ}\end{pmatrix}\right]=0, \tag{36}$$

where $\mathbf{0}$ is a $N\times N$ null matrix. The generalized eigenvalues $\bar{p}^2$ of the above generalized eigenvalue problem define the boundaries between the stable and unstable regions and can be computed easily using any commercially available eigenvalue package.

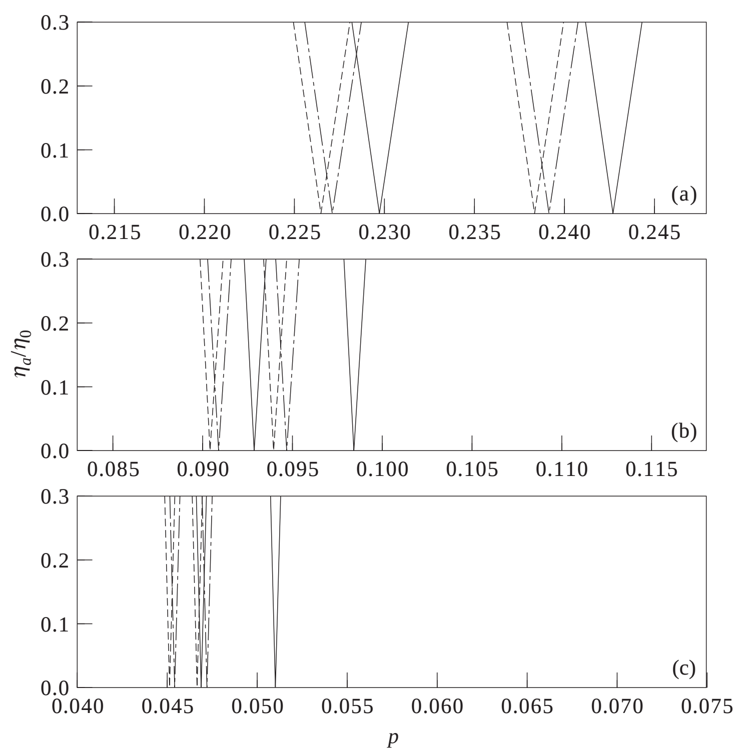

Figure 4. The first two unstable regions for a shell of thickness ratio $R/h = 110$ and under tensile loading of $\eta_0 = 0{\cdot}1\eta_{cr}$. —, Donnell, ----, Love, · · · · · , Sanders, –·–·–, Flugge. (a) $L/R=2$; (b) $L/R = 5$; (c) $L/R = 10$.

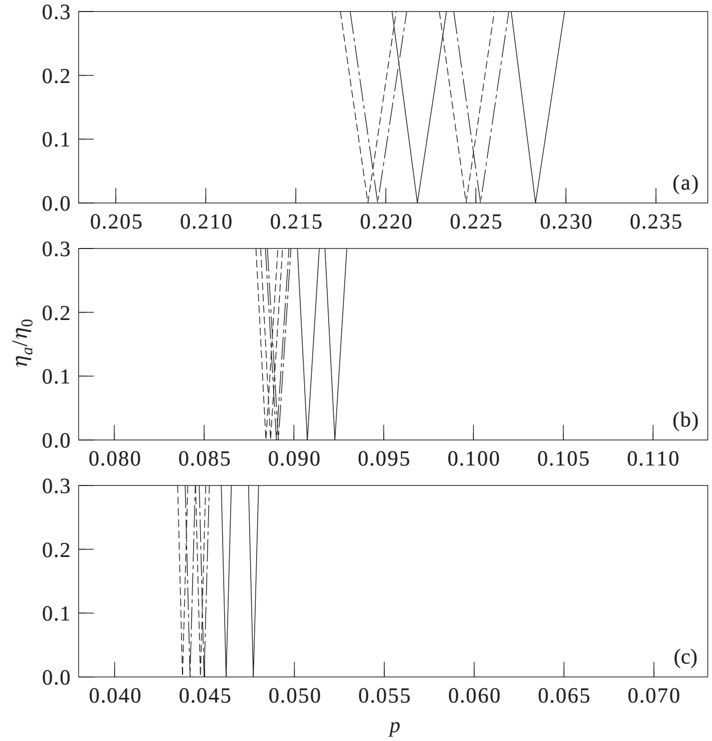

Figure 5. The first two unstable regions for a shell of thickness ratio $R/h = 120$ and under tensile loading of $\eta_0 = 0{\cdot}1\eta_{cr}$. —, Donnell, ——, Love, · · · · · , Sanders, –·–·–, Flugge. (a) $L/R=2$; (b) $L/R = 5$; (c) $L/R = 10$.

4. NUMERICAL RESULTS AND DISCUSSION

The dynamic instability regions for the first order parametric resonances of a circular cylindrical shell under combined static and periodic axial loads are presented in Figure 2–7. It is important to note that for periodic compressive loads, the compressive axial loads cannot exceed the critical buckling load η_{cr} of the cylindrical shell, as this would render the results meaningless. For cylindrical shells of intermediate length, as are the cases used here, the buckling load is given by Timoshenko and Gere [14]

$$P_{cr} = \frac{Eh^2}{[3(1-v^2)]^{1/2}R} \tag{37}$$

and can be non-dimensionalized as

$$\eta_{cr} = P_{cr}\left(\frac{1-v^2}{Eh}\right). \tag{38}$$

If v is taken to be 0·3,

$$\eta_{cr} = 0{\cdot}5507h/R. \tag{39}$$

For the present results, the Poisson ratio v is taken to be 0·3. Each unstable region is bounded by two curves originating from a common point from the $\bar{p}$ axis with $\eta_a = 0$. The two curves appear at first glance to be straight lines, but are in fact very slightly ‘‘outward’’ curving plots. For the sake of tabular presentation, the angle subtended, Θ, is introduced.

TABLE 2

The first two unstable regions for a shell of thickness ratio $R/h = 110$ and under tensile loading of $\eta_0 = 0{\cdot}1\eta_{cr}$

		First unstable region	Second unstable region
$L/R = 2$			
Donnell	Point of origin, $\bar{p}(\times 10^{-1})$	2·2974519	2·4273046
	Angle subtended, Θ $(\times 10^{-3})$	5·1245751	4·9186403
Love	Point of origin, $\bar{p}$ $(\times 10^{-1})$	2·2647545	2·3835380
	Angle subtended, Θ $(\times 10^{-3})$	5·1976332	5·0079381
Sanders	Point of origin, $\bar{p}$ $(\times 10^{-1})$	2·2639765	2·3827282
	Angle subtended, Θ $(\times 10^{-3})$	5·1993931	5·0096181
Flugge	Point of origin, $\bar{p}$ $(\times 10^{-1})$	2·2718157	2·3923601
	Angle subtended, Θ $(\times 10^{-3})$	5·1818136	4·9897986
$L/R = 5$			
Donnell	Point of origin, $\bar{p}(\times 10^{-2})$	9·2928999	9·8386857
	Angle subtended, Θ $(\times 10^{-3})$	1·8946057	1·8788018
Love	Point of origin, $\bar{p}$ $(\times 10^{-2})$	9·0480686	9·4049959
	Angle subtended, Θ $(\times 10^{-3})$	1·9453175	1·9645375
Sanders	Point of origin, $\bar{p}$ $(\times 10^{-2})$	9·0450386	9·4016249
	Angle subtended, Θ $(\times 10^{-3})$	1·9459575	1·9652335
Flugge	Point of origin, $\bar{p}$ $(\times 10^{-2})$	9·0937763	9·4695067
	Angle subtended, Θ $(\times 10^{-3})$	1·9356816	1·9513335
$L/R = 10$			
Donnell	Point of origin, $\bar{p}(\times 10^{-2})$	4·6919409	5·1104076
	Angle subtended, Θ $(\times 10^{-4})$	8·3331981	8·6552778
Love	Point of origin, $\bar{p}$ $(\times 10^{-2})$	4·5187263	4·6724251
	Angle subtended, Θ $(\times 10^{-4})$	8·6496178	9·4587572
Sanders	Point of origin, $\bar{p}$ $(\times 10^{-2})$	4·5175421	4·6708386
	Angle subtended, Θ $(\times 10^{-4})$	8·6518578	9·4619372
Flugge	Point of origin, $\bar{p}$ $(\times 10^{-2})$	4·5471908	4·7206079
	Angle subtended, Θ $(\times 10^{-4})$	8·5961179	9·3632973

TABLE 3

The first two unstable regions for a shell of thickness ratio $R/h = 120$ and under tensile loading of $\eta_0 = 0{\cdot}1\eta_{cr}$

		First unstable region	Second unstable region
$L/R = 2$			
Donnell	Point of origin, $\bar{p}(\times 10^{-1})$	2·2182939	2·2846596
	Angle subtended, Θ $(\times 10^{-3})$	4·8656016	4·7894234
Love	Point of origin, $\bar{p}$ $(\times 10^{-1})$	2·1898602	2·2456084
	Angle subtended, Θ $(\times 10^{-3})$	4·9280201	4·8717815
Sanders	Point of origin, $\bar{p}$ $(\times 10^{-1})$	2·1891843	2·2448864
	Angle subtended, Θ $(\times 10^{-3})$	4·9295201	4·8733214
Flugge	Point of origin, $\bar{p}$ $(\times 10^{-1})$	2·1959959	2·2534749
	Angle subtended, Θ $(\times 10^{-3})$	4·9145404	4·8550619
$L/R = 5$			
Donnell	Point of origin, $\bar{p}(\times 10^{-2})$	9·0715384	9·2234788
	Angle subtended, Θ $(\times 10^{-3})$	1·7794501	1·8367379
Love	Point of origin, $\bar{p}$ $(\times 10^{-2})$	8·8351535	8·8611305
	Angle subtended, Θ $(\times 10^{-3})$	1·9165997	1·8212640
Sanders	Point of origin, $\bar{p}$ $(\times 10^{-2})$	8·8321387	8·8585309
	Angle subtended, Θ $(\times 10^{-3})$	1·9172457	1·8217900
Flugge	Point of origin, $\bar{p}$ $(\times 10^{-2})$	8·8928609	8·9003581
	Angle subtended, Θ $(\times 10^{-3})$	1·9043277	1·8133480
$L/R = 10$			
Donnell	Point of origin, $\bar{p}(\times 10^{-2})$	4·6147815	4·7639598
	Angle subtended, Θ $(\times 10^{-4})$	7·7682984	8·5090579
Love	Point of origin, $\bar{p}$ $(\times 10^{-2})$	4·3697829	4·4671707
	Angle subtended, Θ $(\times 10^{-4})$	9·2688373	8·0227183
Sanders	Point of origin, $\bar{p}$ $(\times 10^{-2})$	4·3683576	4·4661642
	Angle subtended, Θ $(\times 10^{-4})$	9·2718173	8·0244983
Flugge	Point of origin, $\bar{p}$ $(\times 10^{-2})$	4·4130819	4·4913755
	Angle subtended, Θ $(\times 10^{-4})$	9·1789574	7·9799583

It is calculated based on the arctangent of the right-angled triangle, *abc*, obtained by halving the whole unstable region as shown in Figure 2. This angle gives a good measure of the size of the unstable region, as calculations done with the smaller similar triangle, $ab'c'$ (see Figure 2), are within 0·2%.

The effects of variation of the length-to-radius ratios, l, are presented in Figure 3 for the first two instability regions of a cylindrical shell of radius to thickness ratio, $R/h = 100$, and under a tensile loading of $\eta_0 = 0{\cdot}1\eta cr$. The tabular presentation of Figure 3 is given in Table 1. The coresponding results for thinner shells of $R/h = 110$ and $R/h = 120$ are given in Figures 4 and 5 respectively. The tabular presentations of Figures 4 and 5 respectively are given in Tables 2 and 3. It is observed from these three figures that the points of origin of the unstable regions are lower for the longer shells. This is expected, as the natural frequencies of the cylindrical shell are expected to decrease with an increase in its length, and the points of origin of these primary unstable regions correspond to twice the magnitude of the natural frequencies. Another observation from these three figures is that the sizes of the unstable regions decrease with increased cylinder length. These three figures also show that the points of origin of the unstable regions are lower for the thinner shells, which is expected as the natural frequencies of the cylindrical shell are expected to decrease with decreased thickness. Here, the sizes of the unstable regions decrease very slightly with the decreasing thicknesses. This slight decrease is not immediately apparent to the naked eye but can clearly be observed from the tabular presentations given in Tables 1–3. The preceding observations hold for all the four shell theories used. From

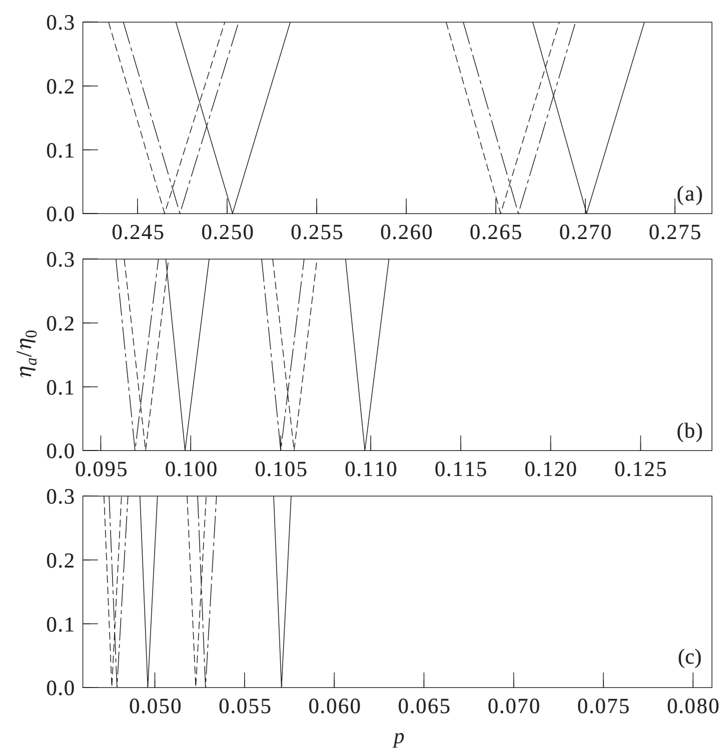

Figure 6. The first two unstable regions for a shell of thickness ratio $R/h = 100$ and under tensile loading of $\eta_0 = 0{\cdot}2\eta_{cr}$. —, Donnell, ----, Love, · · · · · , Sanders, –·–·–, Flugge. (a) L/R=2; (b) $L/R = 5$; (c) $L/R = 10$.

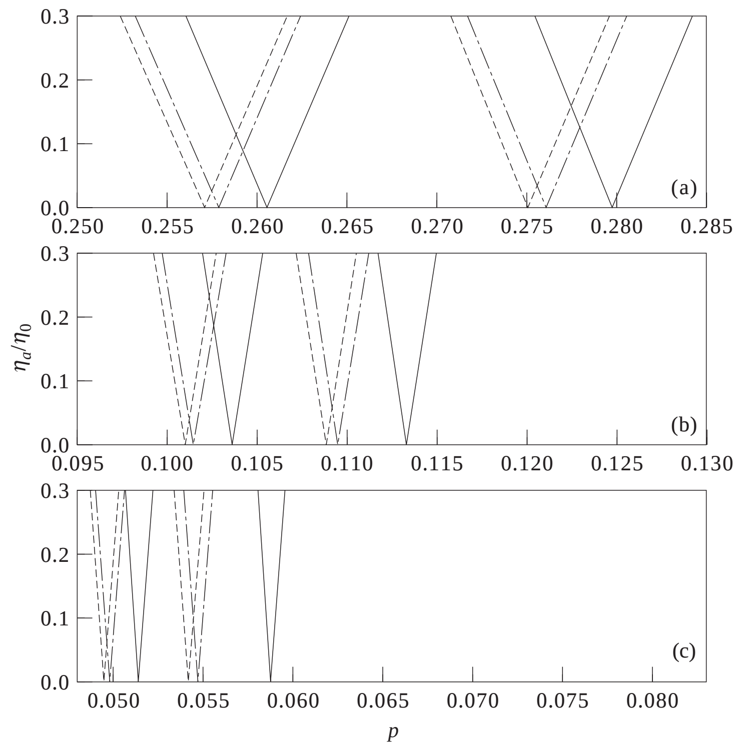

Figure 7. The first two unstable regions for a shell of thickness ratio $R/h = 100$ and under tensile loading of $\eta_0 = 0{\cdot}3\eta_{cr}$. —, Donnell, ----, Love, · · · · · , Sanders, –·–·–, Flugge. (a) $L/R=2$; (b) $L/R = 5$; (c) $L/R = 10$.

Figures 3, 4 and 5, it is observed that the points of origins of the unstable regions obtained from the four shell theories, with the exception of the Donnell theory, agree well with each other. This trend regarding the relative accuracies between the four shell theories was also observed and reported by Lam and Loy [13] in the free vibration analysis of rotating laminated cylindrical shells. Although not obvious from Figures 3–5, the tabular presentations of Tables 1–3 also shows that the results for the sizes of the unstable regions obtained from the four shell theories, with the exception of the Donnell theory, agree well with one another. It is also observed that as the length ratio L/R increases, the agreement between the Donnell theory and the other three theories deteriorates. This was also noted by Lam and Loy [13] in the free vibration analysis.

The effects of variation of the magnitude of the axial loading, η_0 are examined in Figures 3, 6 and 7. In Figures 6 and 7 are presented the results for loadings of $\eta_0 = 0{\cdot}2$ and $\eta_0 = 0{\cdot}3$ respectively. The tabular presentations of Figures 6 and 7 respectively are given in Tables 4 and 5. It is observed from these three figures that the points of origin of the unstable regions are higher for higher magnitudes of tensile loadings, η_0. This is expected, as a higher tensile loading will cause the cylindrical shell to become, stiffer thus increasing the natural frequencies. The respective sizes of the instability regions are observed to increase with increased magnitudes of the tensile loadings. The increase in the sizes of these regions is proportional to the increase in the magnitudes of the loadings, as can be clearly seen from Tables 1, 4 and 5.

TABLE 4

The first two unstable regions for a shell of thickness ratio $R/h = 100$ and under tensile loading of $\eta_0 = 0{\cdot}2\eta_{cr}$

		First unstable region	Second unstable region
$L/R = 2$			
Donnell	Point of origin, $\bar{p}(\times 10^{-1})$	2·5029288	2·7016491
	Angle subtended, Θ $(\times 10^{-2})$	1·0299856	0·9684317
Love	Point of origin, $\bar{p}$ $(\times 10^{-1})$	2·4666034	2·6540732
	Angle subtended, Θ $(\times 10^{-2})$	1·0448200	0·9854601
Sanders	Point of origin, $\bar{p}$ $(\times 10^{-1})$	2·4657386	2·6531928
	Angle subtended, Θ $(\times 10^{-2})$	1·0451779	0·9857761
Flugge	Point of origin, $\bar{p}$ $(\times 10^{-1})$	2·4744543	2·6636677
	Angle subtended, Θ $(\times 10^{-2})$	1·0416083	0·9820044
$L/R = 5$			
Donnell	Point of origin, $\bar{p}(\times 10^{-1})$	0·9971025	1·0969024
	Angle subtended, Θ $(\times 10^{-3})$	3·8669167	3·6939832
Love	Point of origin, $\bar{p}$ $(\times 10^{-1})$	0·9694727	1·0498603
	Angle subtended, Θ $(\times 10^{-3})$	3·9748951	3·8565409
Sanders	Point of origin, $\bar{p}$ $(\times 10^{-1})$	0·9691305	1·0494948
	Angle subtended, Θ $(\times 10^{-3})$	3·9762650	3·8578609
Flugge	Point of origin, $\bar{p}$ $(\times 10^{-1})$	0·9746351	1·0568555
	Angle subtended, Θ $(\times 10^{-3})$	3·9543614	3·8315612
$L/R = 10$			
Donnell	Point of origin, $\bar{p}(\times 10^{-2})$	4·9670320	5·7053933
	Angle subtended, Θ $(\times 10^{-3})$	1·7244763	1·7001364
Love	Point of origin, $\bar{p}$ $(\times 10^{-2})$	4·7687453	5·2313409
	Angle subtended, Θ $(\times 10^{-3})$	1·7948701	1·8516079
Sanders	Point of origin, $\bar{p}$ $(\times 10^{-2})$	4·7673874	5·2296262
	Angle subtended, Θ $(\times 10^{-3})$	1·7953721	1·8522039
Flugge	Point of origin, $\bar{p}$ $(\times 10^{-2})$	4·8013761	5·2834271
	Angle subtended, Θ $(\times 10^{-3})$	1·7829281	1·8337039

TABLE 5

The first two unstable regions for a shell of thickness ratio $R/h = 100$ and under tensile loading of $\eta_0 = 0{\cdot}3\eta_{cr}$

		First unstable region	Second unstable region
$L/R = 2$			
Donnell	Point of origin, $\bar{p}$ ($\times 10^{-1}$)	2·6049126	2·7976571
	Angle subtended, Θ ($\times 10^{-2}$)	1·4787122	1·3978549
Love	Point of origin, $\bar{p}$ ($\times 10^{-1}$)	2·5700271	2·7517399
	Angle subtended, Θ ($\times 10^{-2}$)	1·4981899	1·4205684
Sanders	Point of origin, $\bar{p}$ ($\times 10^{-1}$)	2·5691970	2·7508905
	Angle subtended, Θ ($\times 10^{-2}$)	1·4986558	1·4209943
Flugge	Point of origin, $\bar{p}$ ($\times 10^{-1}$)	2·5775665	2·7609981
	Angle subtended, Θ ($\times 10^{-2}$)	1·4939788	1·4159694
$L/R = 5$			
Donnell	Point of origin, $\bar{p}(\times 10^{-1})$	1·0354108	1·1335415
	Angle subtended, Θ ($\times 10^{-3}$)	5·5651025	5·3440091
Love	Point of origin, $\bar{p}$ ($\times 10^{-1}$)	1·0088303	1·0880841
	Angle subtended, Θ ($\times 10^{-3}$)	5·7076580	5·5617427
Sanders	Point of origin, $\bar{p}$ ($\times 10^{-1}$)	1·0085014	1·0877315
	Angle subtended, Θ ($\times 10^{-3}$)	5·7094580	5·5634826
Flugge	Point of origin, $\bar{p}$ ($\times 10^{-1}$)	1·0137933	1·0948361
	Angle subtended, Θ ($\times 10^{-3}$)	5·6806389	5·5284237
$L/R = 10$			
Donnell	Point of origin, $\bar{p}(\times 10^{-2})$	5·1380325	5·8741770
	Angle subtended, Θ ($\times 10^{-3}$)	2·4920948	2·4694250
Love	Point of origin, $\bar{p}$ ($\times 10^{-2}$)	4·9466042	5·4149192
	Angle subtended, Θ ($\times 10^{-3}$)	2·5861102	2·6739756
Sanders	Point of origin, $\bar{p}$ ($\times 10^{-2}$)	4·9452951	5·4132626
	Angle subtended, Θ ($\times 10^{-3}$)	2·5867762	2·6747736
Flugge	Point of origin, $\bar{p}$ ($\times 10^{-2}$)	4·9780725	5·4652597
	Angle subtended, Θ ($\times 10^{-3}$)	2·5702203	2·6499858

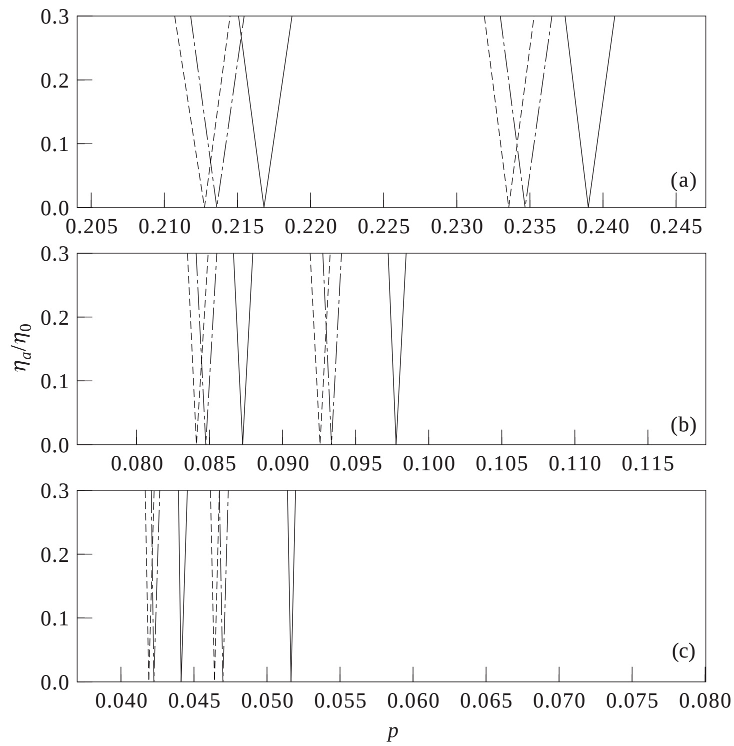

Figure 8. The first two unstable regions for a shell of thickness ratio $R/h = 100$ and under compressive loading of $\eta_0 = -0{\cdot}1\eta_{cr}$. —, Donnell, ----, Love, · · · · · , Sanders, –·–·–, Flugge. (a) $L/R = 2$; (b) $L/R = 5$; (c) $L/R = 10$.

Figures 8–12 are the corresponding results for compressive loadings of Figures 3–7. Contrary to the tensile cases, the points of origin of the unstable regions are lower for higher magnitudes of compressive loadings, η_0. However, this is expected as a higher compressive loading will cause the cylindrical shell to become less stiff, thus decreasing the natural frequencies. Apart from this, the preceding observations for the tensile cases were also observed for the compressive cases. The trend regarding the relative accuracies between the four shell theories observed in the tensile cases was also observed for the compressive cases. An interesting observation which can be made at this point is that for the same magnitude of tensile and compressive loadings, the instability regions generated from the compressive loadings are generally larger than those generated from tensile loadings.

5. CONCLUSIONS

The dynamic stability of simply supported, thin, isotropic cylindrical shells under combined static and periodic axial forces has been investigated using four different shell theories—those due to Donnell, Love, Sanders and Flugge—based on a method in which

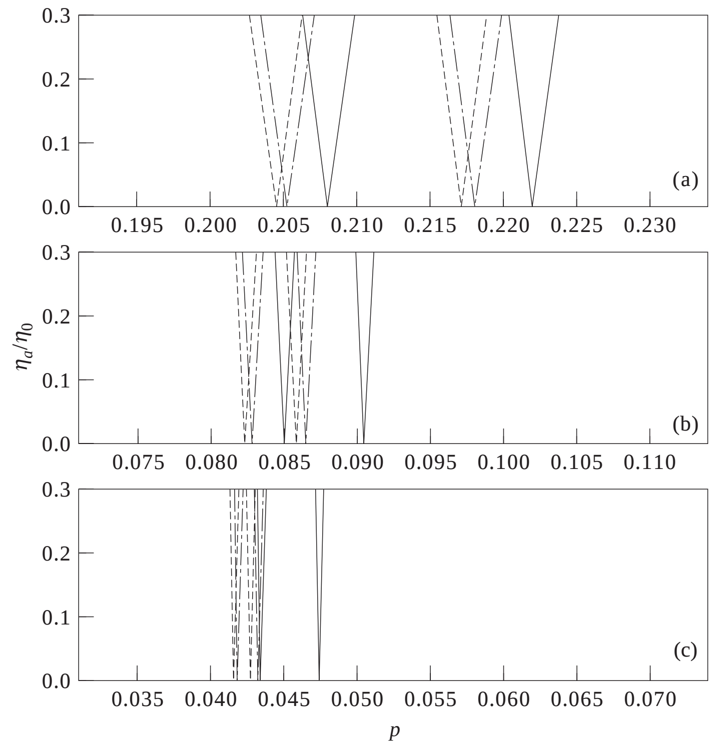

Figure 9. The first two unstable regions for a shell of thickness ratio $R/h = 110$ and under compressive loading of $\eta_0 = -0{\cdot}1\eta_{cr}$. —, Donnell, ----, Love, · · · · · , Sanders, –·–·–, Flugge. (a) $L/R = 2$; (b) $L/R = 5$; (c) $L/R = 10$.

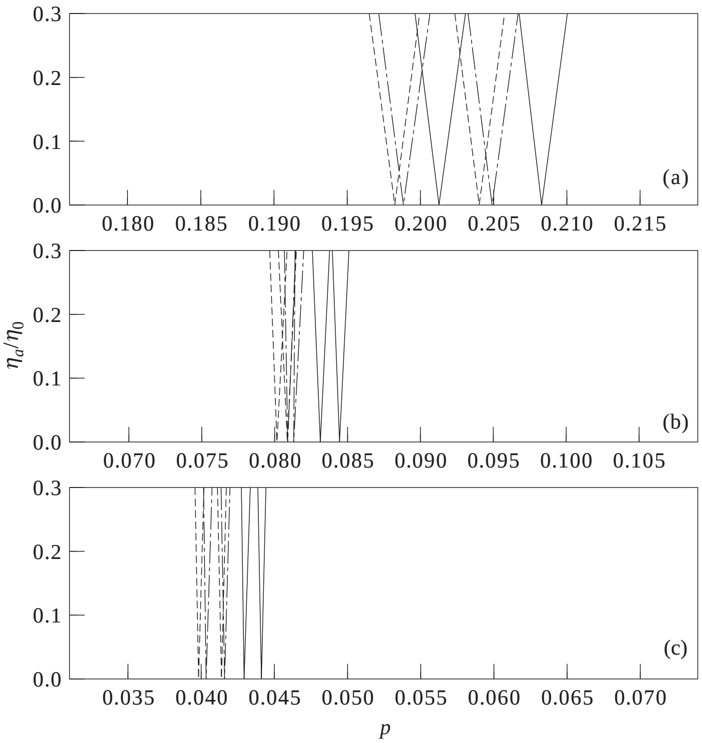

Figure 10. The first two unstable regions for a shell of thickness ratio $R/h = 120$ and under compressive loading of $\eta_0 = -0{\cdot}1\eta_{cr}$. —, Donnell, ----, Love, · · · · ·, Sanders, –·–·–, Flugge. (a) $L/R=2$; (b) $L/R = 5$; (c) $L/R = 10$.

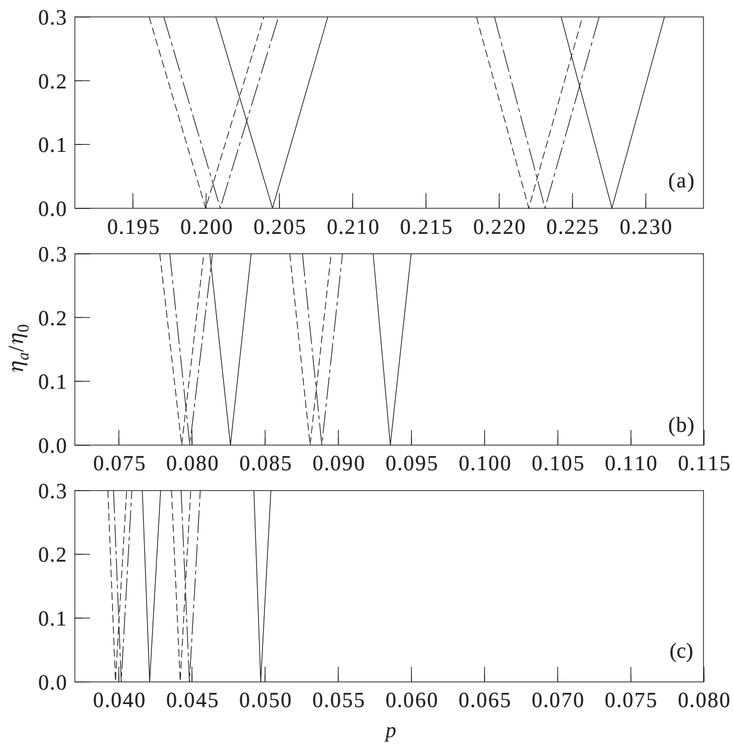

Figure 11. The first two unstable regions for a shell of thickness ratio $R/h = 100$ and under compressive loading of $\eta_0 = -0{\cdot}2\eta_{cr}$. —, Donnell, ----, Love, · · · · · , Sanders, –·–·–, Flugge. (a) $L/R = 2$; (b) $L/R = 5$; (c) $L/R = 10$.

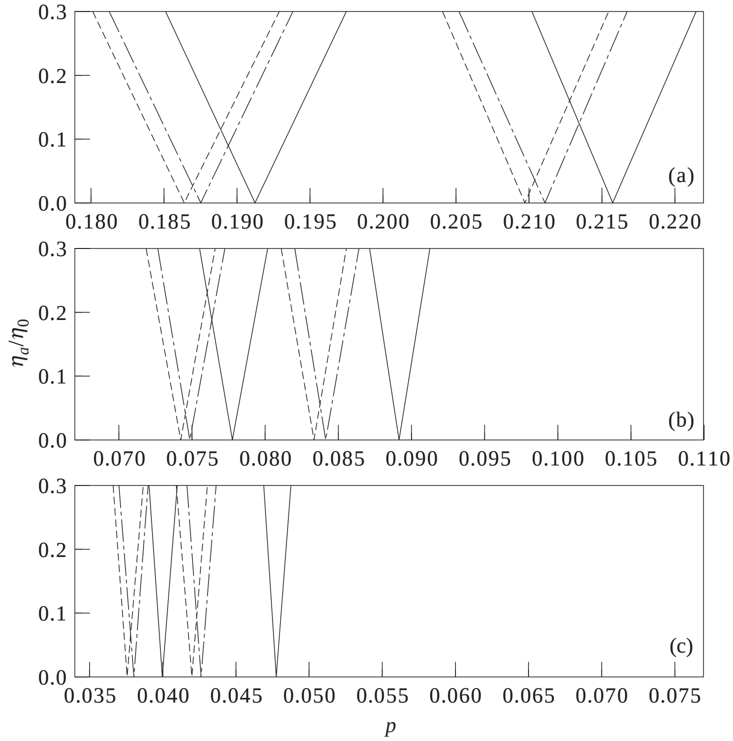

Figure 12. The first two unstable regions for a shell of thickness ratio $R/h = 100$ and under compressive loading of $\eta_0 = -0{\cdot}3\eta_{cr}$. —, Donnell, ----, Love, · · · · ·, Sanders, –·–·–, Flugge. (a) $L/R = 2$; (b) $L/R = 5$; (c) $L/R = 10$.

a system of Mathieu–Hill equations were obtained via a normal-mode expansion and the parametric resonance response was analyzed using Bolotin's method. In the four cases, the contribution of the stresses due to the external axial forces are accounted for according to the Donnell theory. Numerical results have been presented for simply supported circular cylindrical shells subjected to a periodic tensile and compressive axial loadings well below the static critical buckling load of the shell. Of the four shell theories used, it was found that three of them—those due to Love, Sanders and Flugge—agreed well with one another.

REFERENCES

1. V. V. Bolotin 1964 *The Dynamic Stability of Elastic Systems*. San Francisco: Holden-Day.
2. J. C. Yao 1965 *Transactions of the American Society of Mechanical Engineers*, *Journal of Applied Mechanics* **29**, 109–115. Nonlinear elastic buckling and parametric excitation of a cylinder under axial loads.
3. A. Vijayaraghavan and R. M. Evan-Iwanowski 1967 *Transactions of the American Society of Mechanical Engineers*, *Journal of Applied Mechanics* **31**, 985–990. Parametric instability of circular cylindrical shells.
4. L. R. Koval 1974 *Journal of the Acoustical Society of America* **55**, 91–97. Effect of longitudinal resonance on the parametric stability of an axially excited cylindrical shell.
5. A. Argento and R. A. Scott 1993 *Journal of Sound and Vibration* **162**, 311–322. Dynamic instability of layered anisotropic circular cylindrical shells, part I: theoretical development.
6. A. Argento and R. A. Scott 1993 *Journal of Sound and Vibration* **162**, 323–332. Dynamic instability of layered anisotropic circular cylindrical shells, part II: numerical results.

7. A. Argento 1993 *Journal of Composite Materials* **27**, 1722–1738. Dynamic stability of a composite circular cylindrical shell subjected to combined axial and torsional loading.
8. K. Takahashi and Y. Konishi 1988 *Journal of Sound and Vibration* **123**, 115–127. Dynamic stability of a rectangular plate subjected to distributed in-plane dynamic force.
9. K. Takahashi, Y. Natsuaki and Y. Konishi 1991 *Journal of Sound and Vibration* **146**, 211–221. Dynamic stability of a circular arch subjected to distributed in-plane dynamic force.
10. K. Nagai and N. Yamaki 1978 *Journal of Sound and Vibration* **58**, 425–441. Dynamic stability of circular cylindrical shells under periodic compressive forces.
11. K. Y. Lam and C. T. Loy 1995 *International Journal of Solids and Structures* **32**, 647–663. Free vibrations of a rotating multi-layered cylindrical shell.
12. K. Y. Lam and C. T. Loy 1995 *Journal of Sound and Vibration* **188**, 363–384. Effects of boundary condition on the frequency characteristics for a multi-layered cylindrical shell.
13. K. Y. Lam and C. T. Loy 1995 *Journal of Sound and Vibration* **186**, 23–35. Analysis of rotating laminated cylindrical shells using different shell theories.
14. S. P. Timoshenko and J. M. Gere 1961 *Theory of Elastic Stability*. New York: McGraw-Hill.

APPENDIX A

A.1. DONNELL

$$\beta_{mnj} = \frac{n(2\Omega^2 - (1-v)(n^2 + \lambda^2(2+v)))}{(\Omega^2 - \lambda^2 - n^2)(2\Omega^2 - (1-v)(\lambda^2 + n^2))},$$

$$\Gamma_{mnj} = \frac{\lambda((1-v)(v\lambda^2 - n^2) - 2v\Omega^2)}{(\Omega^2 - \lambda^2 - n^2)(2\Omega^2 - (1-v)(\lambda^2 + n^2))}.$$

A.2. LOVE

$$\beta_{mnj} = \left[-n - k^2(\lambda^2 n + n^3) + \frac{\lambda^2 n v(1+v)}{2\lambda^2 + n^2 - 2\Omega^2 - n^2 v}\right] \Bigg/ \left[n^2 - \Omega^2 + k^2(n^2 + \lambda^2(1-v)) + \frac{\lambda^2(1-v)}{2} - \frac{\lambda^2 n^2 (1+v)^2}{4(\lambda^2 + n^2/2 - \Omega^2 - n^2 v/2)}\right],$$

$$\Gamma_{mnj} = \left[-n - k^2(\lambda^2 n + n^3) + \frac{2(n^2 - \Omega^2 + k^2(n^2 + \lambda^2(1-v)) + \lambda^2(1-v)/2)v}{n + nv}\right] \Bigg/ \left[\frac{-(\lambda n(1+v))}{2} + \frac{2(n^2 - \Omega^2 + k^2(n^2 + \lambda^2(1-v)) + \lambda^2(1-v)/2)(\lambda^2 + n^2/2 - \Omega^2 - n^2 v/2)}{\lambda n(1+v)}\right].$$

A.3. SANDERS

$$\beta_{mnj} = \left[-n - k^2\left(n^3 + \frac{\lambda^2 n(3-v)}{2}\right) + \frac{\lambda^2 n(-4 + 3k^2 - 4v - 3k^2 v)(k^2 n^2 - 2v - k^2 n^2 v)}{16(\lambda^2 + n^2/2 + k^2 n^2/8 - \Omega^2 - n^2 v/2 - k^2 n^2 v/8)}\right] \Bigg/$$

$$\left[n^2 - \Omega^2 + k^2\left(n^2 + \frac{9\lambda^2(1-v)}{8}\right)\right.$$

$$+\frac{\lambda^2(1-\nu)}{2}+\frac{\lambda^2n^2(4-3k^2+4\nu+3k^2\nu)^2}{8(-8\lambda^2-4n^2-k^2n^2+8\Omega^2+4n^2\nu+k^2n^2\nu)}\Bigg],$$

$$\Gamma_{mnj}=\Bigg\{-n-k^2\left(n^3+\frac{\lambda^2n(3-\nu)}{2}\right)+\Bigg[4\left(n^2-\Omega^2+k^2\left(n^2+\frac{9\lambda^2(1-\nu)}{8}\right)\right.$$

$$\left.+\frac{\lambda^2(1-\nu)}{2}\right)(k^2n^2-2\nu-k^2n^2\nu)\Bigg]\Bigg/n(-4+3k^2-4\nu-3k^2\nu)\Bigg\}$$

$$\Bigg/\Bigg\{\frac{3k^2\lambda n(1-\nu)}{8}-\frac{\lambda n(1+\nu)}{2}$$

$$-\frac{8(n^2-\Omega^2+k^2(n^2+9\lambda^2(1-\nu)/8)+\lambda^2(1-\nu)/2)\times(\lambda^2+n^2/2+k^2n^2/8-\Omega^2-n^2\nu/2-k^2n^2\nu/8)}{\lambda n(-4+3k^2-4\nu-3k^2\nu)}\Bigg\}.$$

A.4. FLUGGE

$$\beta_{mnj}=\left[-n+\frac{k^2\lambda^2n(-3+\nu)}{2}-\frac{\lambda n(1+\nu)\,(-(\lambda\nu)+k^2n^2(\lambda-2n-\lambda\nu)/2)}{2\lambda^2+n^2+k^2n^2-2\Omega^2-n^2\nu-k^2n^2\nu}\right]\Bigg/\Bigg[n^2-\Omega^2$$

$$+\frac{\lambda^2(1-\nu)}{2}+\frac{3k^2\lambda^2(1-\nu)}{2}-\frac{\lambda^2n^2(1+\nu)^2}{2(2\lambda^2+n^2+k^2n^2-2\Omega^2-n^2\nu-k^2n^2\nu)}\Bigg],$$

$$\Gamma_{mnj}=\left[-n+\frac{k^2\lambda^2n(-3+\nu)}{2}-\frac{2(n^2-\Omega^2+\lambda^2(1-\nu)/2+3k^2\lambda^2(1-\nu)/2)(-(\lambda\nu)+k^2n^2(\lambda-2n-\lambda\nu)/2)}{\lambda n(1+\nu)}\right]\Bigg/$$

$$\left[\frac{-(\lambda n(1+\nu))}{2}+\frac{(n^2-\Omega^2+\lambda^2(1-\nu)/2+3k^2\lambda^2(1-\nu)/2)\times(2\lambda^2+n^2+k^2n^2-2\Omega^2-n^2\nu-k^2n^2\nu)}{\lambda n(1+\nu)}\right].$$